# Revealing chlorinated ethene transformation hotspots in a nitrate impacted hyporheic zone

Weatherill, John; Krause, Stefan; Ullah, Sami; Cassidy, Nigel; Levy, Amir ; Drifjhout, Falko; Rivett, Michael O.

*DOI:*
10.1016/j.watres.2019.05.083



*Document Version*
Peer reviewed version

*Citation for published version (Harvard):*
Weatherill, J, Krause, S, Ullah, S, Cassidy, N, Levy, A, Drifjhout, F & Rivett, MO 2019, 'Revealing chlorinated ethene transformation hotspots in a nitrate impacted hyporheic zone', *Water Research*, vol. 161, pp. 222-231. https://doi.org/10.1016/j.watres.2019.05.083

# Revealing chlorinated ethene transformation hotspots in a nitrate-impacted hyporheic zone

John J. Weatherill [a*], Stefan Krause [b], Sami Ullah [b] Nigel J. Cassidy [c], Amir Levy [d], Falko P. Drijfhout [e], Michael O. Rivett [f g]

[a] School of Biological, Earth and Environmental Sciences, University College Cork, Cork, Ireland.

[b] School of Geography, Earth and Environmental Science, University of Birmingham, UK.

[c] School of Engineering, University of Birmingham, UK.

[d] Lattey Group, Gisborne & Hawkes Bay, New Zealand.

[e] School of Physical and Geographical Sciences, Keele University, UK.

[f] Ground$H_2O$ plus Ltd., Quinton, Birmingham, UK.

[g] Department of Civil and Environmental Engineering, University of Strathclyde, Glasgow, UK

*Corresponding author email: john.j.weatherill@gmail.com

## Abstract

Hyporheic zones are increasingly thought of as natural bioreactors, capable of transforming and attenuating groundwater pollutants present in diffuse baseflow. An underappreciated scenario in the understanding of contaminant fate hyporheic zones is the interaction between point-source trichloroethene (TCE) plumes and ubiquitous, non-point source pollutants such as nitrate. This study aims to conceptualise critical biogeochemical gradients in the hyporheic zone which govern the export potential of these redox-sensitive pollutants from carbon-poor, oxic aquifers. Within the TCE plume discharge zone, discrete vertical profiling of the upper 100 cm of sediment pore water chemistry revealed an 80% increase in dissolved organic carbon (DOC) concentrations and 20–60 cm thick hypoxic zones (<2 mg $O_2$ $L^{-1}$) within which most reactive transport was observed. A 33% reduction of nitrate concentrations coincided with elevated pore water nitrous oxide concentrations as well as the appearance of manganese and the TCE metabolite *cis*-1,2-dichloroethene (cDCE). Elevated groundwater nitrate concentrations (>50 mg $L^{-1}$) create a large stoichiometric demand for bioavailable DOC in discharging groundwater. With the benefit of a high-resolution grid of pore water samplers investigating the shallowest 30 cm of hypoxic groundwater flow paths, we identified DOC-rich hotspots associated with submerged vegetation (*Ranunculus* spp.), where low-energy metabolic processes such as mineral dissolution/reduction, methanogenesis and ammonification dominate. Using a chlorine index metric, we show that enhanced TCE to cDCE transformation takes place within these biogeochemical hotspots, highlighting their relevance for natural plume attenuation.



**Keywords:** hyporheic zone; terminal electron-accepting processes; chlorinated ethenes; nitrate; dissolved organic carbon; natural attenuation.

## 1 Introduction

Chlorinated ethenes (CEs) such as trichloroethene (TCE) and its metabolites *cis*-1,2-dichloroethene (cDCE) and vinyl chloride (VC) are among the most common volatile organic contaminants (VOCs) detected in groundwater (Shapiro et al., 2004; Rivett et al., 2012, Palau et al., 2014). These organohalides are prominent chemical stressors in surface water ecosystems impacted by legacy industrial sources (Roy et al., 2018; Sonne et al., 2018). Dissolved-phase CE plumes often continue to migrate in aquifers with limited sorption capacity, and frequently discharge with groundwater baseflow to streams and rivers (Weatherill et al., 2018). Back-diffusion from low permeability media to groundwater means that many plumes will continue to persist well into or even beyond this current century (Seyedabbasi et al., 2012). Hence, given their environmental health significance and widespread abundance, it is little surprise that CEs are among the most prevalent VOC class reported in surface water to date (e.g. Yamamoto, 2014; Wittlingerová et al., 2016).

In complex landscapes with long histories of diverse land use practices, the concurrence of multiple groundwater pollution incidences is increasingly common. For instance, the natural attenuation and fate of point-source CE plumes which co-mingle with nitrate ($NO_3^-$) from non-point agricultural sources has not been widely considered at field scale to date (e.g. Bennet et al., 2007; Lu et al., 2017). In recent decades, global groundwater $NO_3^-$ concentrations have been steadily rising as a result of increasing agricultural intensification (Gu et al., 2013; Wang et al., 2016). $NO_3^-$ is a mobile anion which only weakly adsorbs to clay minerals (Meghdadi, 2018), often resulting in high loadings to vulnerable aquifers in agricultural regions (Ascott et al., 2017). This groundwater excess of $NO_3^-$ is a well-known global environmental concern linked to

eutrophication of receiving waters (Boyer et al., 2006) and blue-bay syndrome (methaemoglobinaemia) in drinking water (Addiscott and Benjamin, 2006).

Before reaching surface water, these groundwater pollutants must transit the aquifer-river interface or hyporheic zone (HZ) where groundwater and surface water interact (Boano et al., 2014; Cardenas, 2015). The HZ offers considerable promise as a passive biobarrier for in-situ 'treatment' of a broad range of organic groundwater pollutants (Schaper et al., 2018; Gilevska et al., 2019) including CEs (Weatherill et al., 2018). HZ sediments are often naturally rich in organic matter, resulting in hypoxic or anoxic pore water conditions (Atashgahi et al., 2015) where CEs (such as TCE) and $NO_3^-$ are important terminal electron acceptors (TEAs) in dissimilatory microbial metabolism. Here, fermentation of dissolved organic carbon (DOC) supplies electrons via dissolved hydrogen ($H_2$) which drives a thermodynamic series of terminal electron-accepting processes (TEAPs) (Heimann et al., 2009). Under DOC-limiting conditions, this TEAP succession tends to follow an ecological succession which can be predicted by the Gibb's free energy yield ($\Delta G°$) [kJ $mol^{-1}$] of key redox couples: $O_2 \rightarrow H_2O$ [–238]; $NO_3^- \rightarrow N_2$ [–240]; $Mn^{IV} \rightarrow Mn^{II}$; [–185]; $Fe^{III} \rightarrow Fe^{II}$ [–126]; TCE → cDCE [–121]; cDCE → VC [–101]; $SO_4^{2-} \rightarrow HS^-$[–48]; $HCO_3^- \rightarrow CH_4$ [–32.8] (Wiedemeier et al., 1998; under conditions reported therein).

From a thermodynamic perspective, $NO_3^-$ reduction (denitrification) offers considerably higher free energy yields than reductive dechlorination of TCE and cDCE in heterotrophic metabolism (Weatherill et al., 2018). Hence, we hypothesise that elevated groundwater $NO_3^-$ will detrimentally impact the biogeochemical transformation capacity of HZs where plumes discharge through agriculturally intensive landscapes. To test this hypothesis, the present study aims to conceptualise critical biogeochemical gradients

87 which govern the HZ transformation potential of a TCE plume co-mingled with non-
88 point source $NO_3^-$. We apply a 'bottom-up' (Lansdown et al., 2016) multi-scale
89 hydrochemical monitoring approach to: (a) resolve in-situ biogeochemical gradients
90 controlling chemical fluxes from groundwater (b) identify potential hotspots of multi-
91 pollutant transformation and (c) evaluate the impact of regionally elevated $NO_3^-$
92 concentrations on chlorinated ethene transformation in the HZ.

93 ## 2 Materials and methods

94 ### 2.1 Study area characteristics

95 The study area is located in the lowland River Tern catchment (2° 53 W, 52° 86 N)
96 in Shropshire (UK) where regional land use is dominated by intensive agriculture
97 (Krause et al., 2013). The catchment is underlain by highly permeable Permo-Triassic
98 sandstones with groundwater flow through a high porosity matrix (Shepley and Streetly,
99 2007) (Fig. 1). In this tributary of the River Severn, 76% of long-term river flow is
100 derived from groundwater storage (Marsh and Hannaford, 2008). The present study
101 focuses on a 40 m river reach that has been previously identified as the discharge zone
102 of a deep-seated groundwater TCE plume (Fig. 1) (Weatherill et al., 2014). The
103 unconfined regional sandstone aquifer is unlikely to significantly retard migration of the
104 plume (Smith and Lerner, 2008).

105 ### 2.2 Multi-scale hydrochemical monitoring approach

106 Depth-discrete groundwater samples were collected from four sandstone bedrock
107 boreholes (Fig. 1) in March 2012 with passive grab sampling (HydraSleeve™) under
108 ambient borehole flow conditions (Weatherill et al., 2014). A 40 m reach-scale network
109 of multi-level mini-piezometers (MP1-MP25) (see Supporting Information Appendix A;

Figure S1) deployed in the riverbed were sampled in early August 2012 during a summer baseflow recession period (S2). Reach-scale pore water chemistry samples were extracted using dedicated air-tight syringes from PTFE sample tubes with point screens in contact with sediment at 20, 40, 60, 80 and 100 cm below bed level (S1) (Weatherill et al., 2014). Surface water was collected as grab samples from 20 cm above the bed level from the upstream, mid-point and downstream sections of MP network (S1). To provide a high-resolution horizontal window on shallow pore water chemistry, a rectangular grid (0.6 x 2.8 m) of pore water samplers (PW1-PW13) with point-screens at 5, 10, 20 and 30 cm depth was also included (S1, S2). In-situ luminescent dissolved oxygen (DO) was measured in syringe and grab samples using an optical probe (Hach-Lange, UK) with a detection limit of 0.01 mg $O_2$ $L^{-1}$.

### 2.3 Laboratory analysis

VOC samples were analysed using a headspace GC-MS-SIM method described in Weatherill et al. (2014). Dissolved metabolic gas samples were collected in gas-tight Exetainer (Labco, UK) vials fixed by a 50 mol ZnCl solution to inhibit microbial activity. Methane ($CH_4$) and nitrous oxide ($N_2O$) were determined using $N_2$ headspace GC-FID/μECD (Agilent GC7890A series) equipped with a 1 mL sample loop. Equivalent dissolved phase concentrations were estimated from headspace gas volumetric concentrations using Henry's law (Comer-Warner et al., 2018). Equivalent mass concentration detection limits were <0.01 μg $L^{-1}$ for both gases. This GC method was not suitable to detect ethene, the non-chlorinated end-product of TCE reductive dechlorination.

Nitrate ($NO_3^-$), nitrite ($NO_2^-$), sulfate ($SO_4^{2-}$) and chloride ($Cl^-$), were determined by anion chromatography on a Dionex ICS1000 (Dionex Corporation, UK). Ammonium (as

134 N-$NH_4^+$) was analysed using an automated indophenol blue LCK304 method with a
135 detection limit of 0.015 mg N $L^{-1}$ (Hach-Lange, Germany). Total dissolved iron (Fe),
136 manganese (Mn) and silicon (Si) were determined from inline filtered (0.45 µm) and
137 acidified samples using inductively coupled argon plasma optical emission spectroscopy
138 (ICP–OES) (Varian Vista Pro MPX) with detection limits of <0.1 mg $L^{-1}$ for all elements.
139 DOC samples were filtered inline by 0.7 µm pre-combusted (550 °C) glass-fibre filters to
140 pre-combusted glass sample vials acidified with HCl and analysed on a Shimadzu TOC-
141 Vcpn analyser (Shimadzu Corporation, Japan) with a detection limit of 0.2 mg C $L^{-1}$.

142 **2.4 Data analysis**

143 Statistical analyses were performed with SPSS v19 (IBM, USA). Variable
144 distributions were tested using the Shapiro-Wilk test of normality to determine whether
145 parametric or non-parametric statistics were appropriate. Differences in means
146 between groups were analysed using paired T-tests or one-way analysis of variance
147 (ANOVA) for normally or log-normally distributed variables. All means reported were
148 back-transformed from their logarithms. Non-parametric Mann-Whitney U-tests were
149 used to test differences in medians for datasets which were neither normally nor log-
150 normally distributed. Principal component analysis (PCA) was performed on a subset of
151 pore water samples (n = 27) from the high-resolution pore water grid (S1, S2). PCA is
152 advocated as a key line of evidence for biogeochemical interpretation of aquifer CE
153 natural attenuation potential in recent guidance literature (Tarnawski et al., 2015).

154 **3 Results and discussion**

155 **3.1 Aquifer hydrochemistry**

156 Groundwater chemistry results are presented in Table 1. cDCE, VC, Fe, Mn $NH_4^+$ and

157 $NO_2^-$ were all below their detection limits and are not shown. TCE was the only CE
158 detected in the sandstone aquifer with the highest concentrations observed at the 80 m
159 deep HGA abstraction borehole, approximately 500 m distance from the river (Fig. 1).
160 The persistently elevated TCE concentrations (>150 μg $L^{-1}$) at depth in this open
161 borehole are believed to be representative of a deep-seated bedrock plume (Weatherill
162 et al., 2014). The plume is inferred to have a migration pathway along a curved axis
163 between the HGA/HGO boreholes in the up-gradient aquifer and HBE/HBW boreholes
164 on the riverbank (Fig. 1) (Weatherill et al., 2014). The groundwater environment of the
165 up-gradient plume was rich in high-energy TEAs including DO (median: 5.6 mg $L^{-1}$) and
166 $NO_3^-$ (median: 55.3 mg $L^{-1}$) with moderate concentrations of $SO_4^{2-}$ (median: 34.2 mg $L^{-1}$).
167 Groundwater $NO_3^-$ was notably elevated in the riverbank boreholes (73–81 mg $L^{-1}$).
168 Dissolved $N_2O$ was oversaturated by up to 35 times for all groundwater samples with a
169 median concentration of 18 μg $L^{-1}$. The highest $N_2O$ levels (up to 47 μg $L^{-1}$) were
170 associated with the shallower depths of the up-gradient sandstone aquifer. DOC
171 concentrations were very low in the aquifer (<2 mg $L^{-1}$), with highly undersaturated
172 dissolved $CH_4$ concentrations with respect to air equilibrium (<0.1 μg $L^{-1}$).

173 **3.2 Vertical chemical gradients in the hyporheic zone**

174 An overview of maximum pore water TCE and cDCE concentrations in the
175 uppermost metre of riverbed sediment are presented in Fig. 2 with all CE results
176 reported in Supporting Information Appendix B (supplementary tables). cDCE was
177 detected in 10 samples with a maximum of 6.9 μg $L^{-1}$ at MP7 at 40 cm. VC was only
178 confirmed twice at 20 cm in MP18 (0.5 μg $L^{-1}$) and at MP23 (0.7 μg $L^{-1}$). This plume
179 spatial variability in the riverbed sediments is consistent with previous monitoring
180 results in the discharge zone (Weatherill et al., 2014).

Vertical depth-chemistry profiles are presented in Fig. 3 with comparison of pore water median concentrations at the base (100 cm) and top (20 cm) of the riverbed sediment sequence reported in Table 2. We assume that groundwater discharge through the HZ is predominantly vertical and that observed chemical gradients represent bulk attenuation along groundwater flow paths through riverbed pore water pathways (Krause et al., 2013). TCE concentrations exhibited an overall decline during transport through the HZ. High-energy TEAs (DO and $NO_3^-$) and $SO_4^{2-}$ concentrations in deep (100 cm) riverbed pore water samples were similar to the underlying aquifer (Table 2). A step change in DO concentrations from 60–40 cm to shallower sample depths with hypoxic conditions (e.g. <2 mg $O_2$ $L^{-1}$) was observed for many MP locations including the cross-channel TA transect and MP18-23 (Fig. 2).

$NO_3^-$ concentrations declined by one third from the aquifer median during discharge through the HZ. Samples from a group of mini-piezometers (MP12, MP15 and MP16) exhibited exceptionally high $NO_3^-$ concentrations (>130 mg $L^{-1}$) which were not associated with the up-gradient plume (Table 1). Overall, groundwater flow paths through the HZ were not a net source of dissolved $N_2O$ in the plume discharge zone. However, six hypoxic samples from 20 to 40 cm depth had elevated $N_2O$ concentrations (>200 µg $L^{-1}$) including MP6, MP7, MP18 and MP23. $SO_4^{2-}$ concentrations did not vary significantly during transport through the HZ.

Pathways through the HZ were observed to be a significant source of DOC and $CH_4$ with marked increases from 40–20 cm for DOC and 60–40 cm for $CH_4$. These samples coincide with the hypoxic locations at Transect TA and MP18-MP23 and detections of dissolved Mn (up to 9.6 mg $L^{-1}$) and occasionally Fe. Under the near-neutral groundwater pH conditions (Table 1), soluble Fe and Mn are assumed to be mostly a

product of microbially-mediated dissolution/reduction of $Fe^{III}/Mn^{IV}$ mineral phases present in the sediment solids (Tarnawski et al., 2015).

The multi-level chemical profiles obtained at MP7, MP18 and MP223 (Fig. 2) were co-located with 100 cm sediment core samples from Weatherill et al. (2014). These cores provide a physical context for observed biogeochemical gradients below the sediment-water interface (Fig. 4). At each location, discrete changes in biogeochemical conditions takes place in the upper 20 to 60 cm layer of sediment, which is composed of medium sands (MP18 and MP23) and silty peat (MP7). Here, large declines in DO and $NO_3^-$ are associated with elevated DOC, $CH_4$ and $N_2O$ and the appearance of Mn and cDCE (Figs. 2 and 3). Our observations suggest that these hypoxic zones in the HZ can deplete high-energy TEAs from groundwater sufficiently to enable lower energy TEAPs to proceed allowing limited reductive dechlorination of TCE to cDCE.

### 3.3 High-resolution pore water sampler grid

A consistently reactive hypoxic zone was selected for a follow up high-resolution investigation using a rectangular grid pore water samplers (S2). The spatial variability of selected parameters are presented in S3 with all results reported in Appendix B (Table T1). The grid was designed to target horizontal chemical gradients in the area of MP7 (Fig. 4) where the highest cDCE concentrations have been observed in previous work (Weatherill et al., 2014). The riverbed within the grid area was composed of medium quartz sands influenced by submerged macrophyte cover (*Ranunculus* spp.). Comparison of solute concentration means between 5, 10 and 20 cm sample depths using single factor ANOVA did not reveal any statistically significant 'depth effect' ($p = >0.05$) between depth-grouped samples. These results confirm that the sampler network had intercepted pore water above the critical vertical redox gradient in the HZ

(Figs. 3 and 4).

TCE was present in all but four samples within the network with a maximum of 29 μg $L^{-1}$ at PW7 10 cm. cDCE was detectable in 75% of samples with six locations exceeding the MP network maximum of 7 μg $L^{-1}$ (Fig. 4) reaching up 16 μg $L^{-1}$ at PW9 5 cm. VC was above detection limit in 27% of samples with a maximum of 2.3 μg $L^{-1}$ also at PW9 5 cm. All PW samples had DO concentrations ≤2 mg $O_2$ $L^{-1}$ with little variation across the network. $NO_3^-$ was more spatially variable than DO reaching a maximum of 33 mg $L^{-1}$ at PW5 10 cm. This high energy TEA was below detection limit in 13% samples with a further 34% showing $NO_3^-$ less than 5 mg $L^{-1}$. $N_2O$ was spatially variable with concentrations exceeding 100 μg $L^{-1}$ in six samples mostly located in the upstream samplers. Very low concentrations of $N_2O$ (<1 μg $L^{-1}$) were associated with locations which were also characterised by low $NO_3^-$ concentrations in the downstream group of samples. These samplers also exhibited elevated $NH_4^+$ (>1 mg N $L^{-1}$). $SO_4^{2-}$ exhibited a greater range of concentrations than $NO_3^-$ with a maximum of 66.4 mg $L^{-1}$ at PW1 10 cm. This $SO_4^{2-}$ concentration is comparable to the overlying river water (Table 1) and may indicate surface water infiltration to the HZ at the upstream samplers.

Many samples from the downstream group of samplers exhibited DOC concentrations considerably exceeding 10 mg $L^{-1}$ that of river water (Table 2) and those from the MP network (Table 2, Figs. 3 and 4). As a product of low energy mineral-reducing TEAPs, dissolved Mn was widespread with a large number of downstream samples exhibiting Mn concentrations (>10 mg $L^{-1}$). Fe was also present with a range of 1–4 mg $L^{-1}$ and a maximum of 12.7 mg $L^{-1}$ at PW11 30 cm. Many samples from the downstream part of the network exhibited $CH_4$ concentrations in excess of 1000 μg $L^{-1}$ or more than twice that of the MP network maximum (Fig. 3).

Paired two sample T-tests were used to compare spatial means from paired upstream (PW1–PW5) and downstream (PW9–PW13) sample locations (Table 3). Significant declines ($p = <0.05$) are observed from upstream to downstream samples for TCE, $NO_3^-$ and $N_2O$ coupled with significant increases in DOC, Mn and $CH_4$. These results suggest that high and low energy TEAPs may be spatially organised at sub-metre horizontal scales within shallow HZ sediments.

### 3.4 Evaluating in-situ plume transformation extent

The chlorine index (CI) is a useful metric integrating the stoichiometric mass balance of parent compound to daughter products into a single number (Harkness et al., 2012; Freitas et al., 2015). The CI negates the confounding effects of dilution and dispersion to evaluate parent compound transformation extent:

$$CI_{TCE} = \frac{\sum W_i C_i}{\sum C_i}$$

Where $W_i$ is the number of chlorine atoms in the CE molecule and $C_i$ is the molar concentration of the CE species present. The CI approach is a cost-effective alternative to compound-specific stable isotope analysis (CSIA) (e.g. Gilevska et al., 2019) for single-parent compound plumes (Freitas et al., 2015) such as the one is this study. The relationship between total plume mass (in nmol) and $CI_{TCE}$ are presented in Fig. 5 (samples where $CI_{TCE} = 3$ are omitted for clarity). Because it was not possible to include ethene, the minimum $CI_{TCE}$ possible is 1 in this study. From this figure, it can be seen that all mini-piezometer (blue squares) and many samples from the upstream plot-scale grid (open circles) show similar weak dechlorination extents with $CI_{TCE}$ values >2.5 (partial TCE to cDCE transformation). A greater degree of TCE dechlorination is indicated for most samples from the downstream (black circles) and some mid-point samples (green circles) with a $CI_{TCE}$ 1.6 – 2.5 (Fig. 5) where much of the plume mass is transformed to

277 cDCE with limited cDCE reduction to VC.

278 **3.5 Principal component analysis of pore water chemistry**

279 Here, we use PCA to interpret the hypoxic biogeochemical environment in which
280 reductive dechlorination occurs with concomitant TEAPs that cycle nitrogen, carbon,
281 sulfur and minerals in the HZ (Tarnawski et al., 2015). PC1 and PC2 (Fig. 6) represent
282 linear combinations of the original variables from 27 PW network samples which
283 explain 73% of the observed variance. PC1 explains 44.3% and strongly associated with
284 Mn (r = 0.92), Si (r = 0.91), $CH_4$ (r = 0.84), $NH_4^+$ (r = 0.8) and to a lesser extent DOC (r =
285 0.63). PC1 is interpreted as a biogeochemical *metabolite factor* associated which is co-
286 linear with the end-products of low energy TEAPs. This factor is spatially associated
287 with most downstream and some mid-point sample locations, where pore water
288 chemistry is dominated by mineral dissolution, $Mn^{IV}$ reduction and methanogenesis.
289 Although $NH_4^+$ is strongly correlated, PC1 is unrelated to $NO_3^-$ which suggests that
290 ammonification of organic matter is the dominant nitrogen cycling process rather than
291 dissimilatory nitrate reduction to ammonium (DNRA) (Rivett et al., 2008). PC1
292 negatively correlates with $CI_{TCE}$ (r = –0.73) and to a lesser degree $SO_4^{2-}$ (r = –0.6). Hence,
293 in this low-energy biogeochemical environment, TCE is a favourable TEA where
294 sediment/pore water hydrochemical interactions are enhanced.

295 PC2 accounts for 28.8% of the variance observed and is strongly associated with
296 oxidised nitrogen species including $NO_2^-$ and $N_2O$ (r = 0.88) and $NO_3^-$ (r = 0.76). Given the
297 depleted $NO_3^-$ concentrations and hypoxic pore water conditions present, $NO_2^-$ and $N_2O$
298 are likely to be intermediates of in-situ denitrification (Rivett et al., 2008; McAleer et al.,
299 2017). $NH_4^+$ only very weakly correlates with this factor (r = 0.34) which suggests that
300 DNRA may play a limited role in this environment. Hence, PC2 is interpreted as a

*denitrification factor* which is spatially associated with most of the upstream and some mid-point samples. This factor is positively correlated with $CI_{TCE}$ (r = 0.47) and negatively correlated with DOC (r = –0.5). PC2 represents active $NO_3^-$ reduction as a high energy TEAP which is spatially independent of low energy carbon, nitrogen and mineral cycling in the HZ.

# 4 Discussion

## 4.1 Large scale hydrochemical gradients in the hyporheic zone

Reach-scale observations from multi-level profiles within the top metre of bed sediments suggest that the HZ is an important sink for high-energy groundwater TEAs (Table 1) with bulk attenuation of 71% for DO and 33% for $NO_3^-$ (Table 2). Pore water TCE concentrations were observed to decline by 44% in the plume discharge zone (Table 2). The deeper riverbed is characterised by discontinuous lenses of peat, clay and silt overlying the bedrock aquifer which may be up to several metres thick (Weatherill et al., 2014). From Fig. 5, clear differences can be seen in the vertical profiles of TCE where peat is absent (MP18) and present (MP7). Given that metabolites (cDCE and VC) were detected in just 9.5% of MP network samples, much of the observed pore water attenuation may be attributed to non-reactive sorptive-diffusive transport processes (e.g. Rivett et al., 2019).

Before reaching surface water, chemical fluxes from groundwater must transit variable thickness bedforms composed of well-sorted quartz sands with porosities of 20% (Weatherill et al., 2014; Weatherill, 2015). Heat flow experiments have shown that this pore water domain is in close hydraulic continuity with the overlying surface water column (Angermann et al., 2012) due to the presence of the flow-confining structures

beneath (Gomez-Velez et al., 2014). Aquifer and river water $Cl^-$ concentrations did not contrast significantly (Fig. 3) and hence $Cl^-$ could not be used as a conservative tracer to delineate hyporheic exchange zone extent (e.g. Freitas et al., 2015). On the other hand, $SO_4^{2-}$ concentrations differed considerably (Fig. 3). Nonetheless, no evidence of surface water mixing to a depth of 20 cm can be seen in the $SO_4^{2-}$ profiles (Fig. 3) under baseflow conditions. This precludes dilution from surface water infiltration as a factor in the observed TCE attenuation under baseflow conditions in the MP network (e.g. Hamonts et al., 2012).

Our findings suggest that in-situ reactive transport takes place within discrete hypoxic envelopes associated with the TA transect MP locations (40–60 cm thick) and MP18–MP23 where it is thinner (20 cm). This biogeochemically active zone is mostly associated with the quartz sands layer and some peat-rich lenses in the underlying cohesive deposits (Fig. 4). At MP6, MP7, MP18 and MP23, step-change declines in $NO_3^-$ are associated with greater than 10-fold increases in pore water $N_2O$ concentrations (>200 μg $L^{-1}$) (Figs. 3 and 4). $N_2O$ production in the HZ is thought to be indicative of partial $NO_3^-$ reduction where pore water residence times are insufficient to allow complete transformation to $N_2$ (Quick et al., 2016). These hypoxic zones are also associated with an 80% increase in pore water DOC concentrations and a greater than 20-fold increase in $CH_4$ from the aquifer background (Table 2). The presence of $CH_4$ and Mn indicate that low-energy TEAPs take place where high energy TEAs are locally depleted (e.g. DO <2 mg $O_2$ $L^{-1}$; $NO_3^-$ <4 mg $L^{-1}$) (Fig. 4). These conditions appear to be capable of supporting partial reductive dechlorination of TCE to cDCE (e.g. $CI_{TCE}$ >2.5) (Fig. 5)..

## 4.2 Evidence of multi-pollutant transformation hotspots

Evidence of discrete horizontal organisation of dissimilatory TEAPs at sub-metre scales was observed within the rectangular grid (Table 3). At the time of sampling, much of the riverbed at the TA transect of the MP network as well as parts of the wider river corridor was occluded by submerged *Ranunculus* spp. stands. In most upstream PW network samples, active denitrification is suggested by depleted $NO_3^-$ concentrations (<4–30 mg $L^{-1}$) with elevated $N_2O$ (>100 µg $L^{-1}$) and $NO_2^-$ (0.4–2 mg $L^{-1}$). In some downstream and some mid-point samples, oxidised nitrogen species are mostly absent and the pore water chemistry is dominated by the metabolites of low-energy TEAPs including mineral dissolution/reduction, methanogenesis and ammonification (Fig. 6). From a thermodynamic perspective, this low-energy metabolic regime presents a favourable environment for plume transformation which is demonstrated by the low chlorine indices observed in the sub-group of PW samples where $CI_{TCE}$ = 1.6–2.5 (Fig. 5). Overall, the reductive dechlorination potential of the hyporheic zone appears to be limited to cDCE production with only minor concentrations of VC detected which is consistent with previous results (Weatherill et al., 2014). This incomplete natural attenuation may be ascribed to the presence of residual DO concentrations, a lack of suitable cDCE dechlorinator populations or competition for reducing equivalents by metal-reducing bacteria (Chambon et al., 2013; Paul et al., 2016). The presence of both $NH_4^+$ and $CH_4$ in hypoxic samples may favour alternative cometabolic pathways for cDCE and VC mineralisation at the interface between hypoxic and oxic flow paths (Mattes et al., 2010). CSIA and molecular microbial techniques may offer additional lines of evidence to elucidate metabolic pathways and the activities of specific degraders (Badin et al., 2016; Ottosen et al., 2019) and are advocated for future work.

DOC concentrations exceeding that of surface water and the underlying pore water (e.g. >10 mg $L^{-1}$) were observed in many PW samples from the PW network. This is consistent with other reports of vegetated riverbeds as important sources of pore water DOC with intensified hotspots of carbon cycling in the HZ as a result (e.g. Trimmer et al., 2009; Ullah et al., 2014). Submerged macrophytes are thought to modify their local aquatic environment by reducing river flow velocities resulting in increased fine sediment deposition in spring and summer months (Sand-Jensen, 1998; Heppel et al., 2009) with a consequent reduction in bed permeability and an increase in contaminant exposure times in reactive zones (Oldham et al., 2013). Our results suggest that the hypoxic sediments at the mid and down-stream parts of the network were influenced by organic-rich fine sediment derived from allochthonous surface water catchment sources (Ballantine et al., 2008), resulting in elevated in pore water DOC, Mn, Si and $NH_4^+$ concentrations. In addition, delivery of root exudate DOC in the rooting zone which cuts across the HZ may play a role in enhanced biogeochemical cycling in vegetated sediments (Ullah et al., 2014). Our observations show that both $N_2O$ and $CH_4$ are useful indicators for hotspots of high and low-energy TEAP activity respectively in the HZ.

### 4.3 Implications of elevated nitrate on TCE transformation potential

The large metabolic energy gain from reduction of $NO_3^-$ implies that when DOC is in excess, denitrification will take place in preference to lower energy reductive dechlorination reactions in the HZ. Liu et al. (2015) demonstrated that $NO_3^-$ additions had an inhibitory effect on low energy TEAPs ($SO_4^{2-}$ reduction and methanogenesis) in sewer sediments. Denitrifying bacteria can maintain pore water $H_2$ thresholds (<0.1 nmol) far lower than necessary for reductive dechlorination (Weatherill et al., 2018). However, considerable overlap in $H_2$ thresholds are observed experimental studies

under metal-reducing conditions with mineral bioavailability playing an important role (Paul et al., 2016). Our findings suggest that reduction of $NO_3^-$ and TCE to cDCE dechlorination occur independently of one another which is supported by the PCA results in Fig. 6.

Egli et al. (2010) suggest a minimum DOC concentration of 2 mg $L^{-1}$ is required to initiate catabolic genes involved in microbial contaminant transformation. Throughout the up-gradient aquifer, DOC concentrations were at or below this threshold (Table 1). The DOC resources required to reduce high-energy groundwater TEAs (DO and $NO_3^-$) are estimated using the following stoichiometry (Tesoriero and Puckett, 2011):

$$CH_2O + O_2 \rightarrow CO_2 + H_2O \qquad [\Delta G° -238 \text{ kJ mol}^{-1}]$$

$$5CH_2O + 4NO_3^- \rightarrow 2N_2 + 4HCO_3^- + CO_2 + 3H_2O \qquad [\Delta G° -240 \text{ kJ mol}^{-1}]$$

With this stoichiometry, it is possible to estimate the regional DOC demand (mg C $L^{-1}$) imposed by high-energy TEAPs at overlapping spatial scales within the monitoring networks. Fig. 7 plots observed DO concentration against high-energy DOC demand from $DO/NO_3^-$ concentrations recorded in samples. Given the limited solubility of $O_2$ in groundwater, the high-energy DOC demand is dominated by the elevated $NO_3^-$ background (Table 1, Fig. 3). By plotting observed DOC concentration for each sample (denoted by the black diamonds) with the calculated DOC demand, it is possible to identify locations in the HZ where DOC is in excess (Fig. 7). $NO_3^-$-DOC stoichiometric relationships exert important controls on groundwater redox conditions that govern nitrogen export patterns at landscape scale (Taylor and Townsend, 2012; Helton et al., 2015). It is clear that the DOC required to reduce elevated groundwater $NO_3^-$ produces an electron donor-limited environment except for a subset of hypoxic PW samples. In these locations, lower-energy metabolism is favoured including reductive dechlorination

of TCE to cDCE. Therefore, elevated $NO_3^-$ levels are likely to impose a critical redox 'buffer' (e.g. Diem et al., 2013) which must first be overcome when CE plumes traverse intensive agricultural regions underlain by vulnerable oxic groundwater systems.

## 5 Conclusions

With the application of a multi-scale 'bottom-up' monitoring approach, we have shown that biogeochemical processes in the HZ can locally modify chemical fluxes and redox conditions in discharging groundwater. Biogeochemically active hypoxic pathways through the uppermost 20–60 cm of sediment pore water are capable of reducing bulk groundwater discharge of $NO_3^-$ by one third. In these zones, active denitrification is indicated by depleted $NO_3^-$ and elevated dissolved $N_2O$ concentrations. Using the chlorine index of TCE as a metric to evaluate in-situ plume transformation, we have shown that enhanced dechlorination of TCE to cDCE occurs locally within DOC-rich hotspots where pore water chemistry is dominated by the end-products of low-energy microbial metabolism (Mn, $CH_4$ and $NH_4$).

Our results highlight the importance of DOC-rich pore water associated with vegetated riverbeds for seasonal ecosystem service provision in the passive 'treatment' of groundwater pollutants discharging from carbon-poor oxic aquifers. This local electron donor excess is capable of overcoming the large stoichiometric demands for carbon resources posed by high background concentrations of $NO_3^-$. Here, an ecological succession of TEAPs is enabled where reductive dechlorination of CE species becomes thermodynamically favoured. Below a critical DOC threshold, reduction of elevated groundwater $NO_3^-$ inhibits the transformation of CEs in dissimilatory microbial metabolism. The inclusion pore water $N_2O$ and $CH_4$ in combination with DO and

traditional redox indicators to identify respective high and low energy microbial metabolic regimes is advocated further.

## 6 Acknowledgements

This research has been supported by Keele University's ACORN scheme and the UK Environment Agency. The authors acknowledge Sophie Comer-Warner (University of Birmingham) for her assistance with dissolved gas calculations. We acknowledge Kevin Voyce and Andrew Pearson of the UK Environment Agency.

## 7 References

Addiscott, T.M., Benjamin, N., 2004. Nitrate and human health. Soil Use Manage. 20 (2), 98–104.

Angermann, L., Krause, S., Lewandowski, J., 2012. Application of heat pulse injections for investigating shallow hyporheic flow in a lowland river. Water Resour. Res., 48 (12).

Ascott, M.J., Gooddy, D.C., Wang, L., Stuart, M.E., Lewis, M.A., Ward, R.S., Binley, A.M., 2017. Global patterns of nitrate storage in the vadose zone. Nat. Commun. 8 (1), 1416.

Atashgahi, S., Aydin, R., Dimitrov, M.R., Sipkema, D., Hamonts, K., Lahti, L., Maphosa, F., Kruse, T., Saccenti, E., Springael, D., Dejonghe, W., 2015. Impact of a wastewater treatment plant on microbial community composition and function in a hyporheic zone of a eutrophic river. Sci. Rep. 5, 17284.

Badin, A., Broholm, M.M., Jacobsen, C.S., Palau, J., Dennis, P., Hunkeler, D., 2016. Identification of abiotic and biotic reductive dechlorination in a chlorinated ethene plume after thermal source remediation by means of isotopic and molecular biology tools. J. Cont. Hydrol. 192, 1–19.

464 Ballantine, D.J., Walling, D.E., Collins, A.L., Leeks, G.J., 2008. The phosphorus content of
465 fluvial suspended sediment in three lowland groundwater-dominated catchments. J.
466 Hydrol. 357 (1-2), 140–151.

467 Bennett, P., Gandhi, D., Warner, S., Bussey, J., 2007. In situ reductive dechlorination of
468 chlorinated ethenes in high nitrate groundwater. J. Hazard. Mater. 149 (3), 568–573.

469 Boano, F., Harvey, J.W., Marion, A., Packman, A.I., Revelli, R., Ridolfi, L., Wörman, A., 2014.
470 Hyporheic flow and transport processes: mechanisms, models, and biogeochemical
471 implications. Rev. Geophys. 52 (4), 603–679.

472 Boyer, E.W., Howarth, R.W., Galloway, J.N., Dentener, F.J., Green, P.A., Vörösmarty, C.J.,
473 2006. Riverine nitrogen export from the continents to the coasts. Global Biogeochem. Cy.
474 20 (1).

475 Cardenas, M.B., 2015. Hyporheic zone hydrologic science: a historical account of its
476 emergence and a prospectus. Water Resour. Res. 51 (5), 3601–3616.

477 Chambon, J.C., Bjerg, P.L., Scheutz, C., Bælum, J., Jakobsen, R., Binning, P.J. 2013. Review
478 of reactive kinetic models describing reductive dechlorination of chlorinated ethenes in
479 soil and groundwater. Biotechnol. Bioeng. 110 (1), 1–23.

480 Comer-Warner, S.A., Romeijn, P., Gooddy, D.C., Ullah, S., Kettridge, N., Marchant, B.,
481 Hannah, D.M., Krause, S., 2018. Thermal sensitivity of CO2 and CH4 emissions varies
482 with streambed sediment properties. Nat. Commun. 9.

483 Diem, S., Von Rohr, M.R., Hering, J.G., Kohler, H.P.E., Schirmer, M., Von Gunten, U., 2013.
484 NOM degradation during river infiltration: Effects of the climate variables temperature
485 and discharge. Water Res. 47 (17), 6585–6595.

Egli, T., 2010. How to live at very low substrate concentration. Water Res. 44 (17), 4826–4837.

Freitas, J.G., Rivett, M.O., Roche, R.S., Durrant, M., Walker, C., Tellam, J.H., 2015. Heterogeneous hyporheic zone dechlorination of a TCE groundwater plume discharging to an urban river reach. Sci. Total Environ. 505, 236–252.

Gilevska, T., Passeport, E., Shayan, M., Seger, E., Lutz, E.J., West, K.A., Morgan, S.A., Mack, E.E., Lollar, B.S., 2019. Determination of in situ biodegradation rates via a novel high resolution isotopic approach in contaminated sediments. Water Res. 149, 632–639.

Gomez-Velez, J.D., Krause, S., Wilson, J.L., 2014. Effect of low-permeability layers on spatial patterns of hyporheic exchange and groundwater upwelling. Water Resour. Res. 50 (6), 5196–5215.

Gu, B., Ge, Y., Chang, S.X., Luo, W., Chang, J., 2013. Nitrate in groundwater of China: Sources and driving forces. Global Environ. Chang. 23 (5), 1112–1121.

Hamonts, K., Kuhn, T., Vos, J., Maesen, M., Kalka, H., Smidt, H., Springael, D., Meckenstock, R.U., Dejonghe, W., 2012. Temporal variations in natural attenuation of chlorinated aliphatic hydrocarbons in eutrophic river sediments impacted by a contaminated groundwater plume. Water Res. 46 (6), 1873–1888.

Harkness, M., Fisher, A., Lee, M.D., Mack, E.E., Payne, J.A., Dworatzek, S., Roberts, J., Acheson, C., Herrmann, R., Possolo, A., 2012. Use of statistical tools to evaluate the reductive dechlorination of high levels of TCE in microcosm studies. J. Cont. Hydrol. 131 (1–4), 100–118.

508 Heimann, A., Jakobsen, R., Blodau, C., 2009. Energetic constraints on H2-dependent
509 terminal electron accepting processes in anoxic environments: a review of observations
510 and model approaches. Environ. Sci. Technol. 44 (1), 24–33.

511 Helton, A.M., Ardón, M., Bernhardt, E.S., 2015. Thermodynamic constraints on the utility
512 of ecological stoichiometry for explaining global biogeochemical patterns. Ecol. Lett. 18
513 (10), 1049–1056.

514 Heppell, C.M., Wharton, G., Cotton, J.A.C., Bass, J.A.B., Roberts, S.E., 2009. Sediment
515 storage in the shallow hyporheic of lowland vegetated river reaches. Hydrol. Process. 23
516 (15), 2239–2251.

517 Krause, S., Tecklenburg, C., Munz, M., Naden, E., 2013. Streambed nitrogen cycling
518 beyond the hyporheic zone: Flow controls on horizontal patterns and depth distribution
519 of nitrate and dissolved oxygen in the upwelling groundwater of a lowland river. J.
520 Geophys. Res. Biogeosci. 118 (1), 54–67.

521 Lansdown, K., Heppell, C.M., Trimmer, M., Binley, A., Heathwaite, A.L., Byrne, P., Zhang,
522 H., 2015. The interplay between transport and reaction rates as controls on nitrate
523 attenuation in permeable, streambed sediments. J. Geophys. Res. Biogeosci. 120 (6),
524 1093–1109.

525 Liu, Y., Sharma, K.R., Ni, B.J., Fan, L., Murthy, S., Tyson, G.Q., Yuan, Z., 2015. Effects of
526 nitrate dosing on sulfidogenic and methanogenic activities in sewer sediment. Water
527 Res. 74, 155–165.

528 Lu, Q., Jeen, S.W., Gui, L., Gillham, R.W., 2017. Nitrate reduction and its effects on
529 trichloroethylene degradation by granular iron. Water Res. 112, 48–57.

Marsh, T.J., Hannaford, J., (Eds.), 2008. UK Hydrometric Register —Hydrological data UK series. Centre for Ecology and Hydrology, Wallingford, UK.

Mattes, T.E., Alexander, A.K. and Coleman, N.V., 2010. Aerobic biodegradation of the chloroethenes: pathways, enzymes, ecology, and evolution. FEMS Microbiol. Rev. 34 (4), 445–475.

McAleer, E.B., Coxon, C.E., Richards, K.G., Jahangir, M.M.R., Grant, J., Mellander, P.E., 2017. Groundwater nitrate reduction versus dissolved gas production: a tale of two catchments. Sci. Total. Environ. 586, 372–389.

Meghdadi, A., 2018. Characterizing the capacity of hyporheic sediments to attenuate groundwater nitrate loads by adsorption. Water Res. 140, 364–376.

Oldham, C.E., Farrow, D.E., Peiffer, S., 2013. A generalized Damköhler number for classifying material processing in hydrological systems. Hydrol. Earth Sys. Sci. 17 (3), 1133–1148.

Ottosen, C.B., Murray, A.M., Broholm, M.M., Bjerg, P.L. 2019. In Situ Quantification of Degradation Is Needed for Reliable Risk Assessments and Site-Specific Monitored Natural Attenuation. Environ. Sci. Technol. 53 (1), 1–3.

Paul, L., Jakobsen, R., Smolders, E., Albrechtsen, H.J., Bjerg, P.L., 2016. Reductive dechlorination of trichloroethylene (TCE) in competition with Fe and Mn oxides—observed dynamics in H2-dependent terminal electron accepting processes. Geomicrobiol. J. 33 (5), 357–366.

Quick, A.M., Reeder, W.J., Farrell, T.B., Tonina, D., Feris, K.P., Benner, S.G., 2016. Controls on nitrous oxide emissions from the hyporheic zones of streams. Environ. Sci. Technol. 50 (21), 11491–11500.

553 Rivett, M.O., Buss, S.R., Morgan, P., Smith, J.W., Bemment, C.D., 2008. Nitrate attenuation
554 in groundwater: a review of biogeochemical controlling processes. Water Res. 42 (16),
555 4215–4232.

556 Rivett, M.O., Turner, R.J., Glibbery, P., Cuthbert, M.O., 2012. The legacy of chlorinated
557 solvents in the Birmingham aquifer, UK: Observations spanning three decades and the
558 challenge of future urban groundwater development. J. Cont. Hydrol. 140, 107–123.

559 Rivett, M.O., Roche, R.S., Tellam, J.H., Herbert, A.W., 2019. Increased organic contaminant
560 residence times in the urban riverbed due to the presence of highly sorbing sediments of
561 the Anthropocene. J. Hydrol. X 3, 100023.

562 Roy, J.W., Grapentine, L., Bickerton, G., 2018. Ecological effects from groundwater
563 contaminated by volatile organic compounds on an urban stream's benthic ecosystem.
564 Limnologica 68, 115–129.

565 Sand-Jensen, K.A.J., 1998. Influence of submerged macrophytes on sediment composition
566 and near-bed flow in lowland streams. Freshw. Biol. 39 (4), 663–679.

567 Schaper, J.L., Seher, W., Nützmann, G., Putschew, A., Jekel, M., Lewandowski, J., 2018. The
568 fate of polar trace organic compounds in the hyporheic zone. Water Res. 140, 158–166.

569 Seyedabbasi, M.A., Newell, C.J., Adamson, D.T., Sale, T.C., 2012. Relative contribution of
570 DNAPL dissolution and matrix diffusion to the long-term persistence of chlorinated
571 solvent source zones. J. Contam. Hydrol. 134, 69–81.

572 Shapiro, S.D., Busenberg, E., Focazio, M.J., Plummer, L.N., 2004. Historical trends in
573 occurrence and atmospheric inputs of halogenated volatile organic compounds in
574 untreated ground water used as a source of drinking water. Sci. Total Environ. 321(1-3),
575 201–217.

576 Shepley, M.G., Streetly, M., 2007. The estimation of 'natural' summer outflows from the
577 Permo-Triassic Sandstone aquifer, UK. Q. J. Eng. Geol. Hydrogeol. 40(3), 213–227.

578 Smith, J.W.N., Lerner, D.N., 2008. Geomorphologic control on pollutant retardation at the
579 groundwater–surface water interface. Hydrol. Process. 22 (24), 4679–4694.

580 Sonne, A.T., Rasmussen, J.J., Höss, S., Traunspurger, W., Bjerg, P.L., McKnight, U.S., 2018.
581 Linking ecological health to co-occurring organic and inorganic chemical stressors in a
582 groundwater-fed stream system. Sci. Total Environ. 642, 1153–1162.

583 Tarnawski, S.-E., Rossi, P., Holliger, C., 2015. Screening of the Bacterial Reductive
584 Dechlorination Potential of Chlorinated Ethenes in Contaminated Aquifers – A Technical
585 Assistance Manual for Assessment of Natural Attenuation of Chloroethenes-
586 Contaminated sites. Available online: http://infoscience.epfl.ch/record/213613

587 Taylor, P.G., Townsend, A.R., 2012. Stoichiometric control of organic carbon–nitrate
588 relationships from soils to the sea. Nature 464 (7292), 1178.

589 Tesoriero, A.J., Puckett, L.J., 2011. O2 reduction and denitrification rates in shallow
590 aquifers. Water Resour. Res. 47 (12).

591 Trimmer, M., Sanders, I.A., Heppell, C.M., 2009. Carbon and nitrogen cycling in a
592 vegetated lowland chalk river impacted by sediment. Hydrol. Process. 23 (15), 2225–
593 2238.

594 Ullah, S., Zhang, H., Heathwaite, A.L., Heppell, C., Lansdown, K., Binley, A., Trimmer, M.,
595 2014. Influence of emergent vegetation on nitrate cycling in sediments of a
596 groundwater-fed river. Biogeochemistry, 118 (1–3), 121–134.

597 Wang, L., Stuart, M.E., Lewis, M.A., Ward, R.S., Skirvin, D., Naden, P.S., Collins, A.L., Ascott,
598 M.J., 2016. The changing trend in nitrate concentrations in major aquifers due to

599 historical nitrate loading from agricultural land across England and Wales from 1925 to
600 2150. Sci. Total Environ. 542, 694–705.

601 Weatherill, J. J., 2015. Investigating the natural attenuation and fate of a trichloroethene
602 plume at the groundwater-surface water interface of a UK lowland river. PhD thesis,
603 Keele University, UK.

604 Weatherill, J., Krause, S., Voyce, K., Drijfhout, F., Levy, A., Cassidy, N., 2014. Nested
605 monitoring approaches to delineate groundwater trichloroethene discharge to a UK
606 lowland stream at multiple spatial scales. J. Cont. Hydrol. 158, 38–54.

607 Weatherill, J.J., Atashgahi, S., Schneidewind, U., Krause, S., Ullah, S., Cassidy, N., Rivett,
608 M.O., 2018. Natural attenuation of chlorinated ethenes in hyporheic zones: a review of
609 key biogeochemical processes and in-situ transformation potential. Water Res. 128,
610 362–382.

611 Wiedemeier, T.D.H., Swanson, M.A., Moutoux, D.E., Gordon, K.,Wilson, J.T., Wilson, B.H.,
612 Kampbell, D.H., Haas, P.E., Miller, R.N., Hansen, J.E., Chapelle, F.H., 1998. Technical
613 Protocol for Evaluating Natural Attenuation of Chlorinated Solvents in Ground Water,
614 IAG: RW57936164. US Environmental Protection Agency, USA.

615 Wittlingerová, Z., Macháčková, J., Petruželková, A., Zimová, M., 2016. Occurrence of
616 perchloroethylene in surface water and fish in a river ecosystem affected by
617 groundwater contamination. Environ. Sci. Pollut. Res. 23 (6), 5676–5692.

618 Yamamoto, K., 2014. Occurrence, Distribution, and Trends of Volatile Organic
619 Compounds in Urban Rivers and Their Estuaries in Osaka, Japan, 1993–2006. Bull.
620 Environ. Contam. Toxicol. 92 (4), 472–477.

## Tables and figure captions

**Table 1:** Permo-Triassic sandstone groundwater hydrochemistry. Refer to Figure 1 for location of monitoring boreholes.

| Borehole ID | pH | EC | DO | TCE | $NO_3$ | $SO_4$ | Cl | DOC | $CH_4$ | $N_2O$ |
|---|---|---|---|---|---|---|---|---|---|---|
| | pH units | µS $cm^{-1}$ | mg $O_2$ $L^{-1}$ | µg $L^{-1}$ | mg $L^{-1}$ | mg $L^{-1}$ | mg $L^{-1}$ | mg C $L^{-1}$ | µg $L^{-1}$ | µg $L^{-1}$ |
| **HGA 35 m** | 7.6 | 623 | 5.1 | 89 | 66.2 | 24.8 | 32.6 | 2.19 | 0.08 | 44.3 |
| **HGA 50 m** | 7.6 | 556 | 6.6 | 137 | 53.1 | 23.1 | 33.0 | 1.64 | 0.09 | 16.1 |
| **HGA 80 m** | 7.5 | 545 | 6.2 | 162 | 66.7 | 20 | 34.2 | 1.35 | 0.08 | 18.1 |
| **HGO 20m** | 7.8 | 498 | 5.6 | 48.8 | 55.3 | 21.2 | 37.9 | 2.01 | 0.09 | 28.3 |
| **HGO 40m** | 7.7 | 502 | 5 | 74.4 | 52.8 | 20.5 | 36.0 | 1.58 | 0.08 | 20 |
| **HBE** | 7.1 | 753 | 6.4 | 26.9 | 81.1 | 28.4 | 29.6 | 2.14 | 0.07 | 5.9 |
| **HBW** | 7.3 | 661 | 6.8 | 9.38 | 73 | 22 | 37.5 | 1.94 | 0.09 | 17.2 |

**Table 2:** Comparison of median solute concentrations using Mann-Witney U-tests from selected mini-piezometer samples at the bottom (100 cm) and top (20 cm) of the hyporheic zone (n = 16) including the aquifer (n = 7) and river (n = 3) for comparison. Significant changes are expressed as percentages.

| **Parameter** | units | **Aquifer** | **$MP_{100cm}$** | **$MP_{20cm}$** | **River** | **Sig. change** | **p** |
|---|---|---|---|---|---|---|---|
| **TCE** | $\mu g\ L^{-1}$ | 74.4 | 21.1 | 12.0 | <0.01 | -43% | 0.01 |
| **DO** | $mg\ O_2\ L^{-1}$ | 6.3 | 6.4 | 1.9 | 9.6 | -71% | <0.01 |
| **$NO_3$** | $mg\ L^{-1}$ | 60.8 | 60.3 | 40.1 | 37.4 | -33% | <0.01 |
| **$SO_4$** | $mg\ L^{-1}$ | 22.6 | 25.4 | 28.1 | 61.0 | - | >0.05 |
| **Cl** | $mg\ L^{-1}$ | 34.2 | 32.3 | 31.6 | 34.3 | - | >0.05 |
| **DOC** | $mg\ C\ L^{-1}$ | 1.98 | 2.6 | 4.7 | 7.96 | +80% | <0.01 |
| **$N_2O$** | $\mu g\ L^{-1}$ | 17.7 | 18.3 | 17.6 | 3.2 | - | >0.05 |
| **$CH_4$** | $\mu g\ L^{-1}$ | 0.08 | 0.17 | 2.86 | 8.22 | +1582% | <0.01 |

632 **Table 3:** Comparison of selected mean solute concentrations at paired
633 upstream/downstream samples of the pore water grid using paired T-tests (n = 14)
634 (standard deviations in parentheses). Significant changes are expressed as percentages.

| **Parameter** | units | **$PW_{upstream}$** | **$PW_{downstream}$** | **Sig. change** | **p** |
|---|---|---|---|---|---|
| **$NO_3$** | mg $L^{-1}$ | 14.1 (2.03) | 5.1 (1.47) | -64% | <0.05 |
| **$SO_4$** | mg $L^{-1}$ | 38.8 (1.38) | 26.5 (1.53) | -32% | 0.032 |
| **Cl** | mg $L^{-1}$ | 29.9 (1.11) | 32.6 (1.06) | - | >0.05 |
| **Mn** | mg $L^{-1}$ | 2.07 (1.89) | 6.11 (3.07) | +195% | <0.05 |
| **DOC** | mg C $L^{-1}$ | 4.53 (1.38) | 6.89 (1.58) | +32% | <0.05 |
| **$N_2O$** | µg $L^{-1}$ | 31.5 (5.43) | 6.93 (4.45) | -78% | <0.05 |
| **$CH_4$** | µg $L^{-1}$ | 11.6 (2.90) | 266.1 (2.15) | +2196% | <0.05 |

635

636

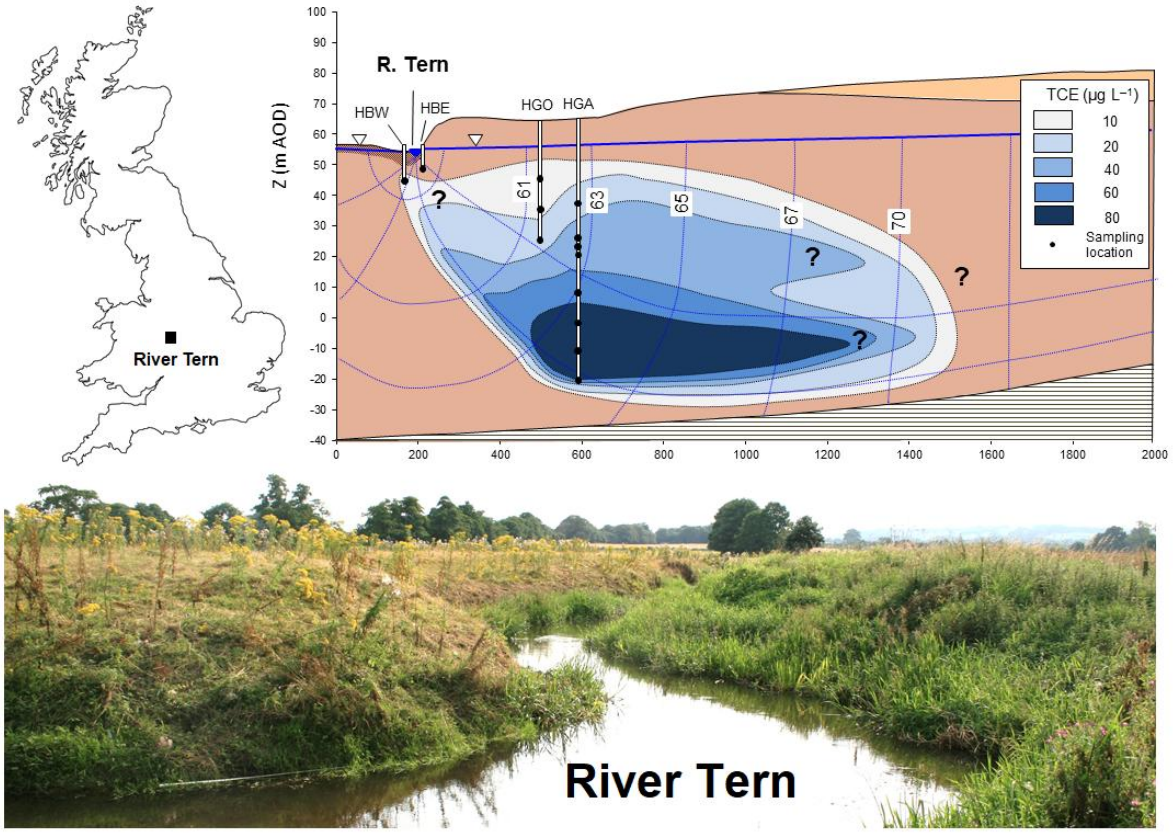


637

638 **Figure 1:** Study area location and conceptual site model of regional aquifer and TCE
639 plume and its inferred discharge zone at the River Tern (adapted from Weatherill et al.,
640 2014). Black dots denote sampling depths in open boreholes using passive methods.

641

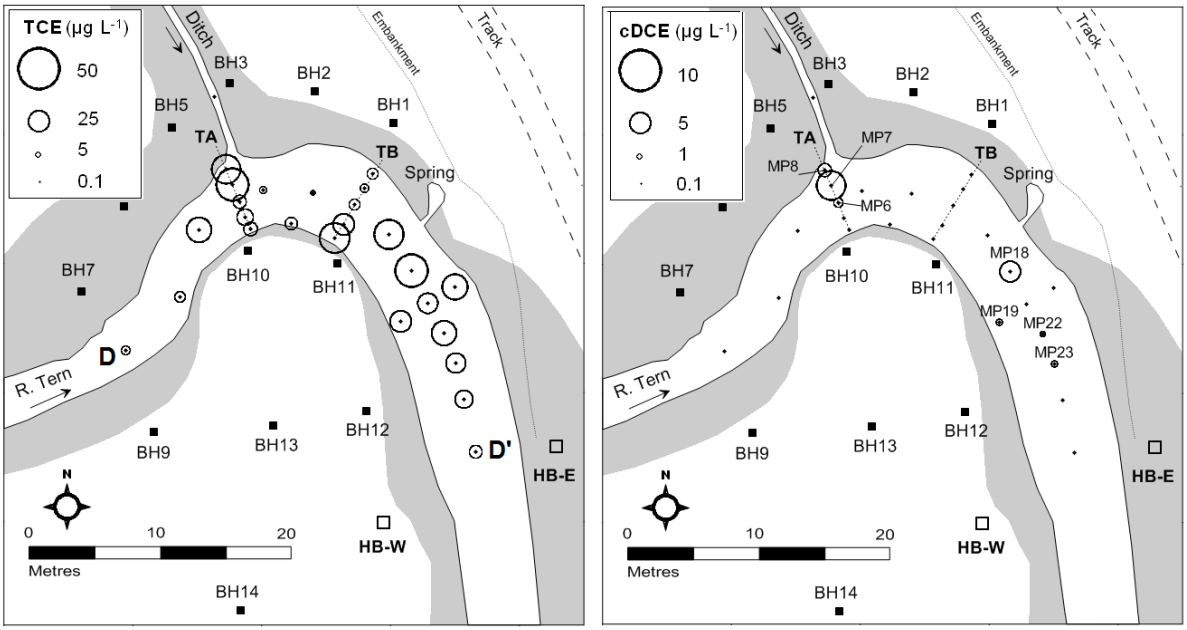


642

643 **Figure 2:** Spatial variability of maximum TCE and cDCE at mini-piezometer locations in
644 the plume discharge zone in August 2012. Cross-channel plume concentration gradients
645 are observed at the TA and TB mini-piezometer transects with the highest TCE
646 concentrations occurring downstream of the TB transect. In-situ reductive
647 dechlorination is indicated by cDCE detections with the highest concentrations at MP7
648 and MP18.

649

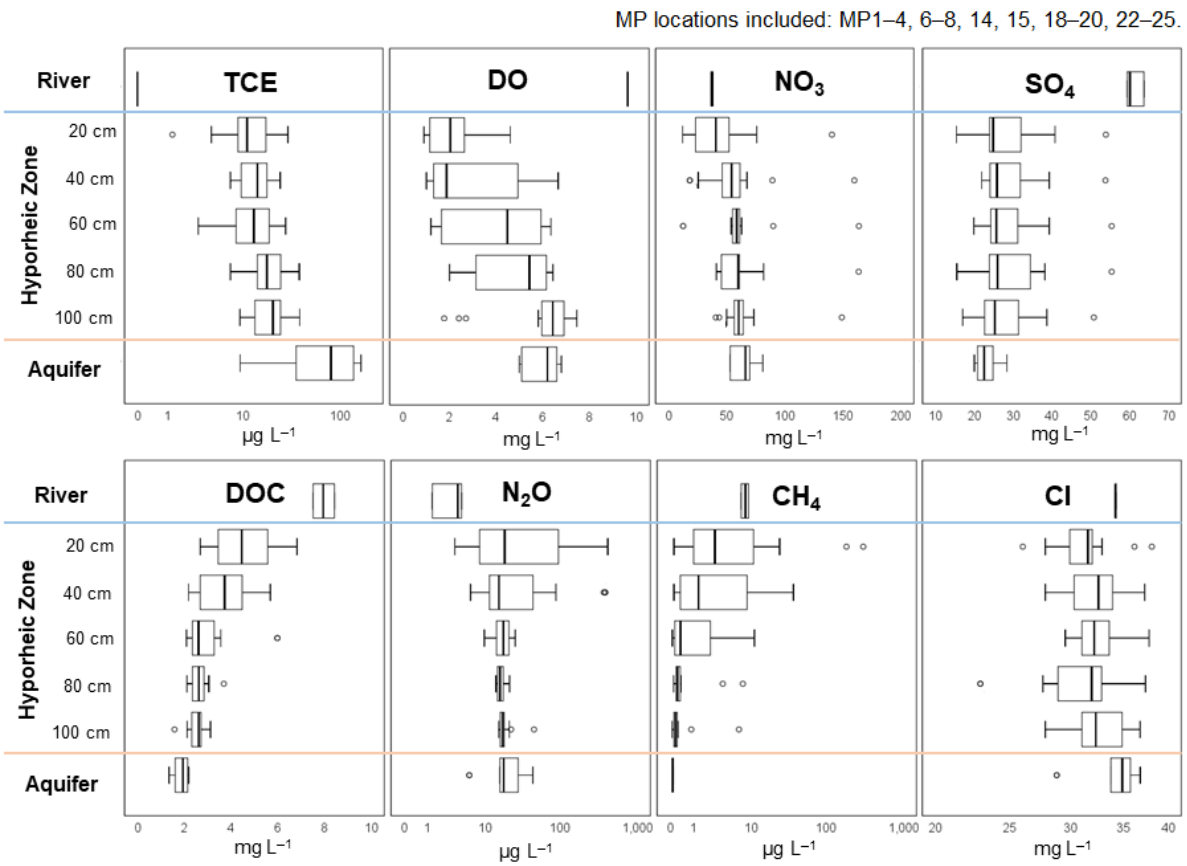


650

651 **Figure 3:** Vertical depth-concentration profiles for mini-piezometer locations used to
652 compare medians (n = 16) in comparison with the up-gradient aquifer (GW) (n = 7) and
653 surface water (SW) (n = 3).

654

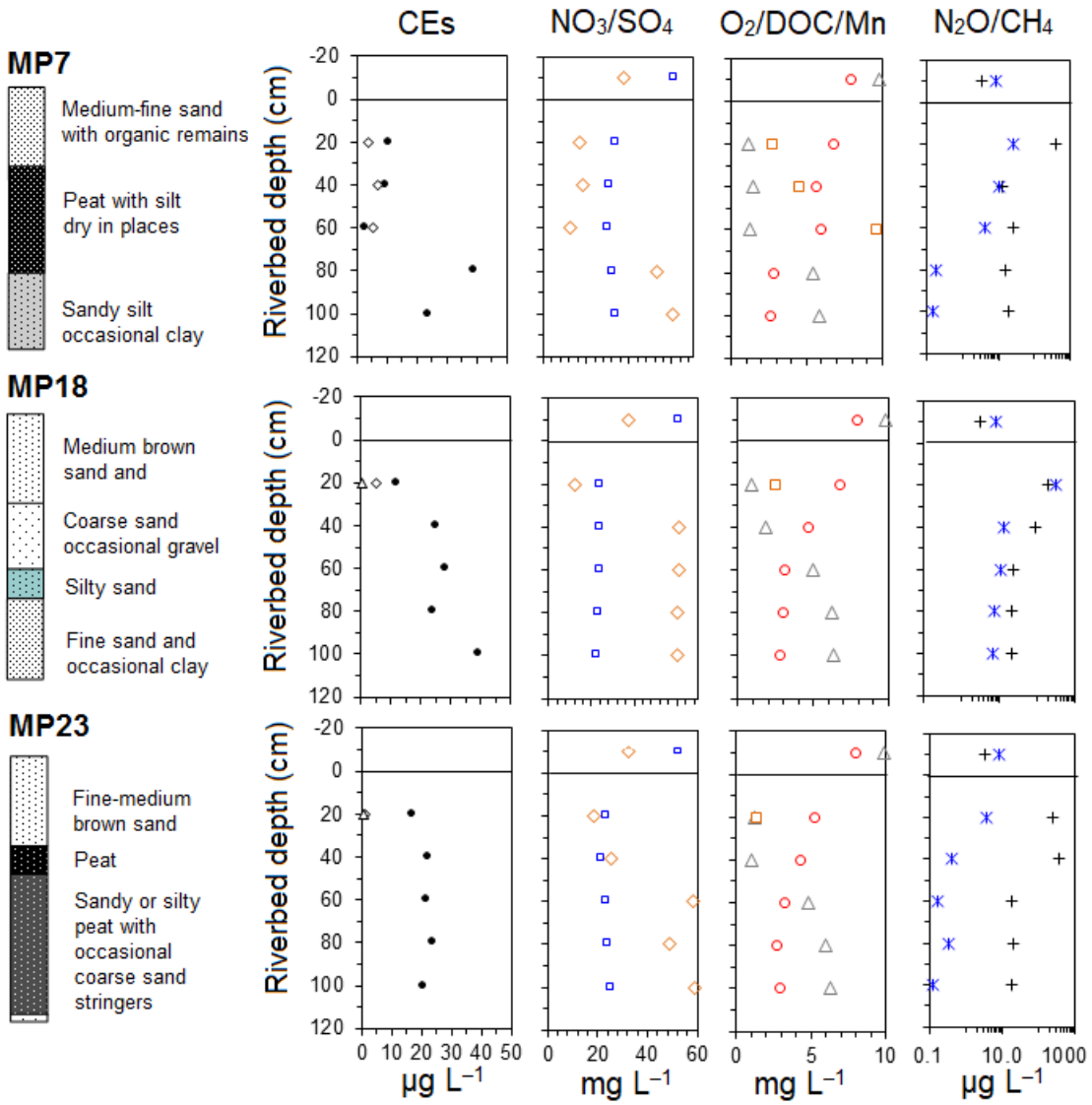


655

656 **Figure 4:** Representative pore water biogeochemical profiles and riverbed sediment
657 properties. TCE (black diamonds); cDCE (open black diamonds); VC (open black
658 triangles); nitrate (open green diamonds); sulfate (open blue squares); DO (open
659 triangles); DOC (open circles), Mn (open orange squares); blue stars (methane) and
660 black crosses (nitrous oxide).

661

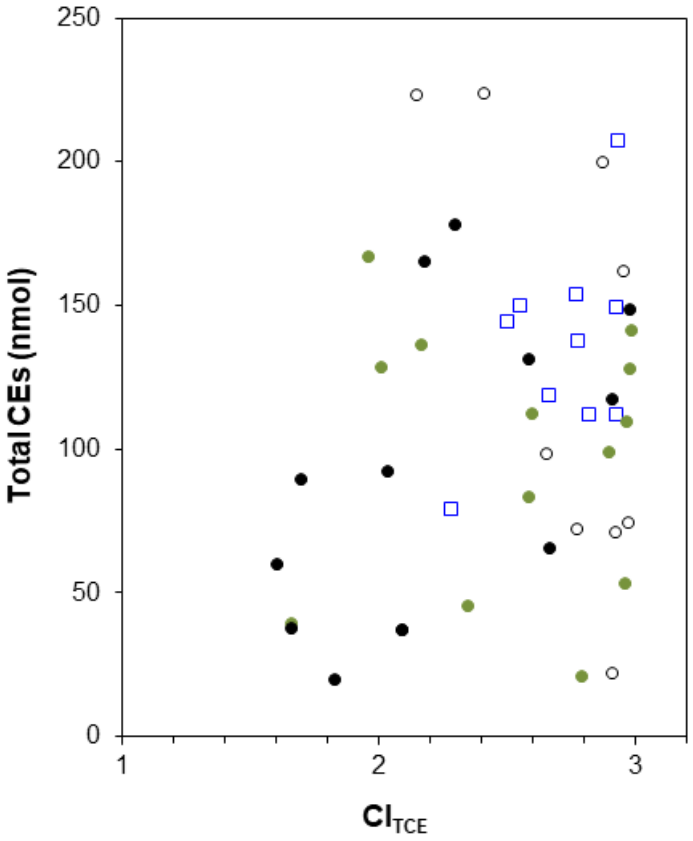


662

663 **Figure 5:** Relationship between total pore water CEs (in nmol) and the chlorine index of
664 TCE ($CI_{TCE}$) in all riverbed samples where $CI_{TCE}$ = <3. Blue squares (reach-scale mini-
665 piezometer samples); open circles (upstream PW samples); green circles (mid-point PW
666 samples); black circles (downstream PW samples).

667

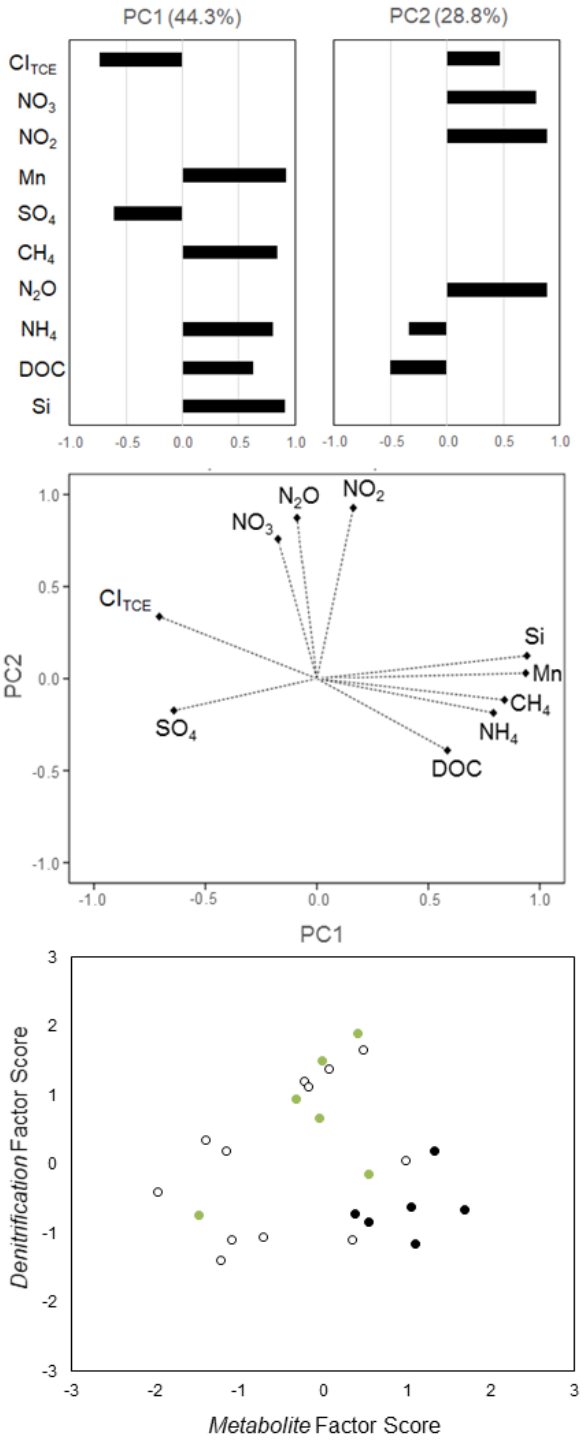


668

669 **Figure 6:** Principle component analysis of high resolution pore water chemistry
670 including factor loadings on original variables, ordination biplot and factor scores. The
671 values in parenthesis is the percentage variance explained by PC1 and PC2. Factor
672 scores are grouped as upstream (open circles), mid-point (green circles) and
673 downstream (black circles) sample locations.

674

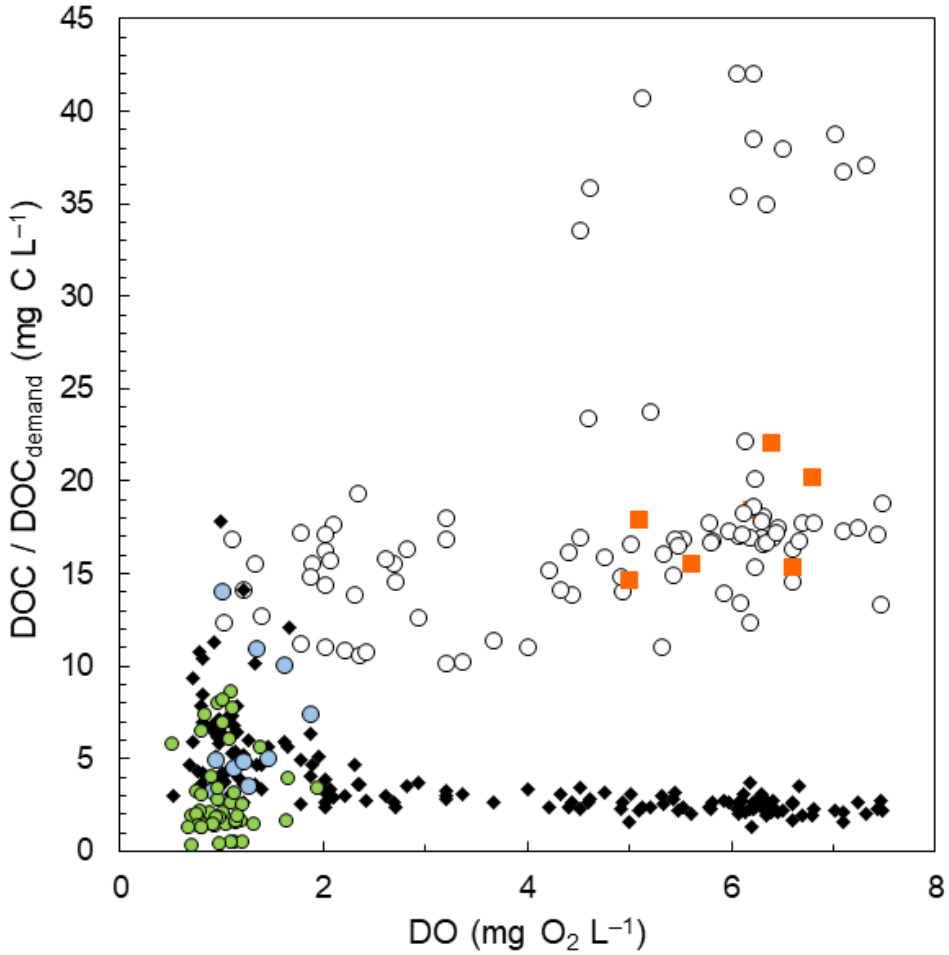


675

676 **Figure 7:** Calculated DOC demand for reduction of dissolved oxygen and nitrate in
677 samples for the sandstone aquifer (orange squares); MP samples (open circles); MP
678 samples showing TCE degradation (blue circles) and PW samples (green circles). Black
679 diamonds denote observed DOC concentrations for each sample.